THE JOURNAL OF PHYSICAL CHEMISTRY C

Article

pubs.acs.org/JPCC

Unraveling the Impurity Location and Binding in Heavily Doped Semiconductor Nanocrystals: The Case of Cu in InAs Nanocrystals

Yorai Amit,[†,‡] Hagai Eshet,[§] Adam Faust,[†,‡] Anitha Patllola,[∥] Eran Rabani,[§] Uri Banin,*[,†,‡] and Anatoly I. Frenkel*[,∥]

[†]The Institute of Chemistry and [‡]The Center for Nanoscience and Nanotechnology, Hebrew University, Jerusalem 91904, Israel

[§]School of Chemistry, Sackler Faculty of Exact Sciences, Tel Aviv University, Tel Aviv 69978, Israel

[∥]The Department of Physics, Yeshiva University, New York, New York 10016, United States

Supporting Information

ABSTRACT: The doping of colloidal semiconductor nanocrystals (NCs) presents an additional knob beyond size and shape for controlling the electronic properties. An important problem for doping with aliovalent elements is associated with resolving the location of the dopant and its structural surrounding within small NCs, an issue directly connected with self-purification. Here we used a postsynthesis diffusion-based doping method for introducing Cu impurities into InAs quantum dots. X-ray absorption fine structure (XAFS) spectroscopy experiments along with first-principle density functional theory (DFT) calculations were used to probe the impurity sites. The concentration dependence was investigated for a wide range of doping levels, helping to derive a self-consistent picture where the Cu impurity occupies an interstitial site within the InAs lattice. Moreover, at extremely high doping levels, Cu−Cu interactions are identified in the XAFS data. This structural model is supported by X-ray diffraction data, along with the DFT calculation. These findings establish the reproducibility of the diffusion-based doping strategy giving rise to new opportunities of correlating the structural details with emerging electronic properties in heavily doped NCs.

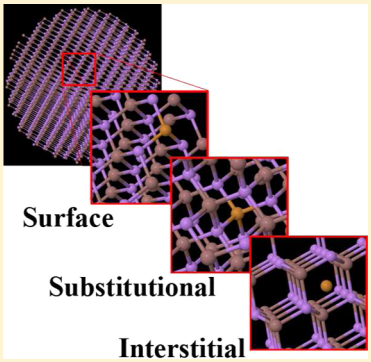

INTRODUCTION

Colloidal semiconductor nanocrystals (NCs) manifest size-dependent optical and electronic properties.[1,2] The variety of materials compatible with colloidal synthesis already includes II−VI,[3] III−V,[4] and IV−VI[5] semiconductor NCs, leading to numerous demonstrations of applications with NC building blocks such as: light emitting diodes,[6] solar cells,[7] sensors, and transistor devices.[8] The field of NCs continues to evolve, producing unique shapes[9,10] and compositions,[11] yet there is an ongoing effort to directly influence the physical properties of the already synthesized nanoparticles by additional wet-chemical means.[12]

The use of impurities (or dopants) is a ubiquitous approach for controlling the physical properties of bulk semiconductors and is the basis for their widespread application in electronic and electro-optic components.[13] In light of this, doping, the process of intentional insertion of impurities, is of great interest for further modification of the behavior of semiconductor NCs.[14−17] Early studies of NC doping focused on isovalent impurities, leading to enhancement of optical and magnetic properties.[18−22] Further modification of properties would emerge from aliovalent doping;[12,14,21−30] however, "self-purification" by which the impurity is expelled to the NC surface may become predominant due to less favorable chemical stabilization of the incompatible impurity.[31−34]

Recently, we have introduced a facile, room-temperature, solution-phase reaction allowing postsynthesis doping of colloidal semiconductor NCs.[12] This diffusion-based doping reaction enabled the synthesis of high-quality doped NCs. A main advantage of this approach is to allow direct comparison of the emerging properties upon introducing different dopants in varying concentrations for a given NC size and composition. Such a diffusion-based doping strategy raises questions in regards to the structural aspects of the end product. Considering that the impurity may be labile, occupy a wide variety of sites, and perhaps even migrate between different sites when already embedded in the NC lattice calls for advanced structural characterization of the system.

Employing this solution-phase reaction, we synthesized *n*-type InAs NCs by doping them with Cu impurities. Furthermore, we previously suggested the Cu to be an interstitial donor given its relatively small size and its mobility in III−V semiconductors.[12] These studies already demonstrated the intricacy of doped NC systems, emphasizing the need for independent identification of the location of the impurity atom embedded in the NC and its structural surrounding.

Received: April 2, 2013
Revised: June 4, 2013
Published: June 4, 2013

   dx.doi.org/10.1021/jp4032749 | J. Phys. Chem. C 2013, 117, 13688−13696

The main challenge in structural characterization of doped NCs lies in their low dimensionality, calling for high spatial resolution that is not available by most characterization techniques. In this work we applied advanced characterization methods of extended X-ray absorption fine structure (EXAFS) and X-ray absorption near edge structure (XANES) spectroscopies, which are complementary methods for local structural characterization and are powerful techniques for studying the electronic and geometric properties of nanoscale materials. This results from the high sensitivity to the local structure surrounding the probed atoms (within 6−8 Å away from the X-ray absorbing atom),[35] the fine spatial resolution in determining the bond length (with uncertainties as low as 0.01 Å or better), the ability to resolve the coordination numbers of nearest neighbors around each absorbing atom, and the sensitivity to the charge state around the absorber.

We present here a combined experimental and computational study of colloidal InAs NCs doped with Cu at various concentrations. Using XANES and EXAFS spectroscopies, we find that the structure surrounding the Cu atoms is independent of impurity concentration for most levels of doping, while the structure surrounding the In and As host atoms changes gradually with dopant concentration. This points to the progressive loading of the InAs structure by interstitially accommodated Cu impurities, with increase in dopant concentrations, while the InAs host structure is generally preserved. The preferred resting site of the Cu impurity within the NC lattice was found to be at a hexagonal interstitial location, which was also confirmed by first-principle density function theory (DFT) calculations. At the highest level of Cu doping, Cu−Cu interactions are identified in the X-ray absorption data, and X-ray diffraction (XRD) data further confirm the structural position of Cu in this limit.

EXPERIMENTAL SECTION

Colloidal InAs NCs. Colloidal InAs nanocrystals were synthesized following a well-established wet-chemical synthesis.[36] Precursor solutions containing mixtures of $(TMS)_3As$ (tris(trimethylsilyl)arsine) and $InCl_3$ (indium(III) chloride) were prepared and kept under inert conditions throughout. A solution of distilled TOP (trioctylphosphine) was evacuated for ∼30 min and heated to 300 °C. The nucleation solution (molar ratio 2:1 In:As) was rapidly injected, and the heating mantle was removed, lowering the solution temperature to 260 °C. The growth solution (1.2:1 In:As) was gradually introduced to the solution, allowing particle growth until the desired size was reached. Narrow size distributions were achieved through size selective precipitation performed in a GB (MBraun) by adding methanol to the NC dispersion and filtering the solution through a 0.2 μm polyamide membrane filter (Whatman). The precipitant was subsequently dissolved in anhydrous-toluene (Sigma) and kept under constant inert conditions throughout.

Doping Presynthesized InAs Nanocrystals. Doping Presynthesized InAs NCs was achieved following a room-temperature solution-phase reaction previously reported by us.[12] In short, an impurity solution was prepared by dissolving the metal salt, that is, copper chloride ($CuCl_2$), didodecyldimethylammonium bromide (DDAB), and dodecylamine (DDA) in anhydrous-toluene (Sigma). The solution was agitated using an ultrasonic bath for ∼30 min to ensure homogeneous conditions. Calculated amounts (v/v) of the impurity solution were added to a InAs NCs suspensions. The doping reaction was performed under an inert condition in a GB (MBraun) while stirring. The reaction was terminated by adding methanol and precipitating the doped NCs. The supernatant containing the unreacted impurities was discarded and the doped NC solution was redissolved in toluene. We note that the Cu/NC ratios reported in the manuscript correspond to the ratio of Cu impurities per NCs for the doping reaction in solution. The actual Cu concentration per NC is derived from this and determined as detailed next.

ICP-AES Measurements. Inductively coupled plasma−atomic emission spectroscopy (ICP-AES) measurements were carried out using a Perkin-Elmer Optima 3000 to determine dopant concentrations within the NCs. The emission signals were collected at 230.6 and 325.6 nm for In ions, 189.0 and 193.7 nm for As ions, and 324.8 and 328.1 nm for Cu. Samples were prepared by dissolving the doped NCs in HNO_3 and diluting the solution with triply distilled water. See the Supporting Information for detailed results.

XAFS Measurements. XAFS measurements were performed at the Brookhaven National Laboratory (BNL) National Synchrotron Light Source (NSLS) beamline X18B. The specimens were prepared under inert conditions in a GB (MBraun), where they were spread on adhesive tape and mounted in a sample chamber. The chamber, filled with nitrogen, was then transferred to the beamline, where it was flushed with nitrogen during the measurements to maintain inert conditions through the experiments. Experiments at the As and In K-edges were performed in transmission mode, and those for Cu K-edge were performed in fluorescence mode. From 3 to 10 consecutive measurements were taken at each edge to improve the signal-to-noise ratio in the data.

XAFS Data Analysis and Processing. XAFS data analysis and processing was done using standard techniques. In brief, the data were first aligned in energy using reference spectra collected in standard materials simultaneously with the NC data and then averaged. Next, the smooth, isolated atom background function was subtracted from the absorption coefficient using Athena program[37] from the IFEFFIT package.[38] Theoretical analysis of the XANES and EXAFS was done by using the linear combination analysis (LCA) program, which is part of Athena. In addition, EXAFS data of Cu were also analyzed by the nonlinear least-squares fitting method incorporated in IFEFFIT.

For Cu K-edge EXAFS fits, theoretical photoelectron scattering amplitudes and phases were calculated using program FEFF6.[39] Adjustable parameters in the theoretical EXAFS signal included the passive electron reduction factor (S_0^2), the coordination numbers of nearest neighbors of a certain type around the absorbing Cu atom (N_i), the bond distance between the absorber and the nearest neighbors (R_i), and its mean-square-displacement (σ_i^2). While the reduction factor was found from the fits to the bulk Cu and fixed in the fits to the doped NC data, the remaining parameters were refined in the fits to the doped NC sample data. With the purpose of improving the reliability of the fit, the fitting process was performed simultaneously for the different doping levels using unique structural variables (N, R, σ^2) for each of the neighboring atom (As,In), for each doping level. The corrections to the photoelectron energy origins were varied independently for Cu−In and Cu−As pair and were global variables for all doping concentrations. In the case of the 2500 Cu doping level, the analysis was modified and described in greater detail below.

dx.doi.org/10.1021/jp4032749 | J. Phys. Chem. C 2013, 117, 13688−13696

Density Functional Theory. Density functional theory calculations were carried out based on the Perdew–Burke–Ernzerhof (PBE) generalized gradient approximation[40] to the exchange and correlation potential with an ultrasoft pseudopotential and a 60 Ry plane-wave basis cutoff in a supercell of 216 In and As atoms. Atomic pseudopotentials include the valence 4d, 5s, and 5p electrons for the In; 4s and 4p electron for the As, and 3d, 4p; and 4s electron for the Cu. The QUANTUMESPRESSO package was used to perform all calculations.[41]

RESULTS AND DISCUSSION

TEM images of the as-synthesized 5 nm (diameter) InAs NCs (Figure 1a) and the heavily doped InAs NCs (Figure 1b) show

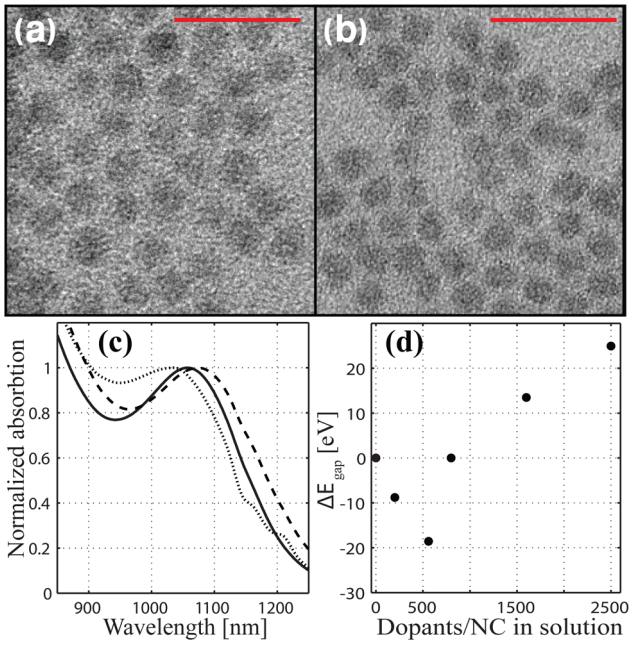

Figure 1. TEM images of (a) 5 nm InAs NCs before and (b) after doping to a level of 1600 Cu atoms/NC in solution (scale bar = 20 nm). (c) Absorption spectra for the undoped 5 nm NCs (solid line), NCs reacted with 560 Cu (dashed line), and 2500 Cu (dotted line). (d) Energy shift of the first exciton peak upon doping the NCs with 200, 560, 800, 1600, and 2500 Cu atoms/QD. (Doping levels indicate the number of Cu atoms per InAs NC in solution. For an estimation of the actual impurity concentrations in the NCs see Table S1 of the Supporting Information.)

that the size and shape of the NCs are preserved upon doping, as previously reported. Figure 1c presents the optical absorption spectra of the undoped (solid line) and Cu-doped (dashed lines) InAs NCs. The absorption onset of the doped samples with respect to the undoped NCs, shown in Figure 1d, initially exhibits a red shift.[42] Upon increasing the dopant concentration, this red shift changes over to an increasing blue shift, assigned to the Moss–Burstein effect,[43] related to conduction and impurity state filling by donated electrons, as discussed in ref 12. Relatively weak band gap emission is observed from the InAs NCs, which is quenched upon doping.

XANES and EXAFS Data. XANES and EXAFS results of the as-synthesized 5 nm InAs NCs and of the NCs with various Cu doping levels are shown in Figure 2. The main peaks in the XANES spectra correspond to the 1s–4p transition energy for Cu and As K-edges and the 1s–5p transition energy for the In K-edge. The peak position is sensitive to the charge state of the absorber. The area under the main peak, known as the "white line" (WL), is related to the density of unoccupied electronic states.[44]

The absorption edge peak positions for In (Figure 2a) and As (Figure 2b) in XANES do not change with Cu doping concentration, indicating that the charge states of both In and As are preserved upon doping. The observed increase in the WL intensity for both In and As with increasing Cu concentration is consistent with an increased number of nearest neighbors. The larger increase observed for the WL of the As-edge (e.g., 60 vs 20%) suggests that the Cu interacts more strongly with the As atoms in the NC. An additional signature, seen for both In and As K-edge XANES regions, is the appearance of isosbestic points (Figure 2a,b). Their presence has been observed numerous times in XAFS experiments and used for the quantitative analysis of mixtures.[45−50] The presence of isosbestic points signifies a one-step transformation between two end configurations, indicating that only one type of Cu site is present in the lattice at all of these doping levels.

The Cu K-edge XANES (Figure 2c) onset of the absorption is shifted to larger energies compared with the Cu^0 standard XANES spectra, toward the peak position of the Cu^+ standard (Figure 2c, inset). This shift is consistent with a positive charge state on the Cu inside the NCs, in agreement with the DFT calculations. In addition, there is a marked increase in intensity at the absorption onset region compared with the spectrum of metallic Cu (as designated by the blue arrow in Figure 2c). This feature signifies an increase in the covalent characteristic of the bonding between the Cu and its nearest neighbors in the NC compared with metallic Cu.[51] Furthermore, both WL intensity and peak position, as measured at the Cu K-edge, are unaffected by the increase in doping levels, in contrast with the large changes observed for In and As K-edges. This indicates that the surrounding of Cu does not change throughout a wide range of Cu concentrations, contrary to the surroundings of both In and As.

Visual examination of the EXAFS data (Figure 2d–f) reinforces the picture depicted by the above XANES interpretation. The peaks in *r* space correspond to the nearest neighbor distances, after correcting for the photoelectron phase shift, which causes the peaks position to decrease by ~0.5 Å relative to the actual interatomic distances.[35] The height of the peak is related to the number of neighbors of a given type and its mean square bond length disorder. For In K-edge (Figure 2d) the EXAFS data manifests a clear isosbestic behavior with a monotonic increase in the low *r*-peak intensity (associated with In–Cu) accompanied by a decrease in the high *r*-peak intensity (associated with In–As) as the Cu concentration increases. Consistent with this trend, the As–In contribution decreases (Figure 2e), while the As–Cu peak increases. However, the relative intensity of the As–Cu versus As–In (Figure 2e) compared with the relative intensity of the In–Cu and the In–As (Figure 2d) is significantly weaker because of the greater Z-contrast between the nearest neighbors in the former case. The Cu EXAFS exhibits relatively small changes with doping levels (Figure 2f), consistent with a single site for the Cu impurities, in agreement with its XANES behavior (vide supra).

We note that, although maintaining the same trends, a change in behavior is observed for the 2500 Cu/NC data compared with the data collected for the lower doping concentrations (Figure 2f). Specifically, the peak is broadened

dx.doi.org/10.1021/jp4032749 | J. Phys. Chem. C 2013, 117, 13688–13696

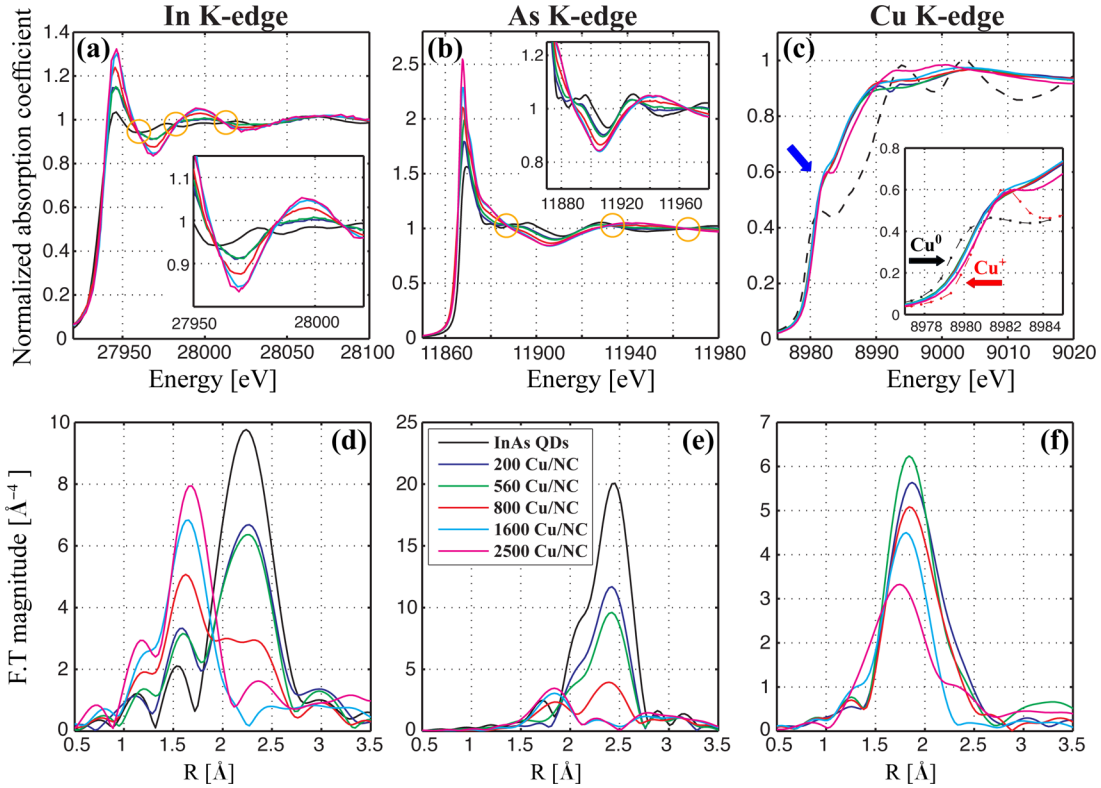

Figure 2. In, As, and Cu K-edge XANES spectra (a–c, respectively) and the Fourier transform (FT) magnitudes of their EXAFS spectra (d–f, respectively) measured for Cu-doped InAs NCs. Dashed lines (c) show the XANES spectra for $Cu^{(0)}$ (black) and Cu^+ (red) standards. The legend in frame (e) refers to all the graphs, and all stated doping levels relate to the doping level in solution.

and shifted to lower r values. The origin of this nonsystematic change will be discussed in the subsequent sections.

Data Analysis and Structural Model for the Impurity Location. As a starting point, we analyzed the structure of the InAs NC by theoretical fitting of As K-edge and In K-edge EXAFS data and found them to be in good agreement with the zincblende structure (Figure S1 and Table S2 of the Supporting Information). To establish the existence of a single site for the Cu impurities within the InAs NC, as borne out from the XANES and EXAFS spectra of all elements (Cu, As, and In), we have calculated theoretically the Cu K-edge EXAFS spectra assuming different structural configurations for the Cu impurity within the InAs lattice. The different structural models, each proposed as a possible impurity site resulting from the diffusion-based doping reaction, were reconstructed based on previous studies of impurity sites within the zincblende structure of the InAs lattice.[52,53] We considered substitutional Cu impurities inside (Figure 3a) or on the surface (Figure 3b) and interstitial Cu impurities occupying tetrahedral (Figure 3c) or hexagonal sites (Figure 2d).

The different models (Figure 3) were then used to fit the experimental EXAFS data collected at the Cu K-edge. The calculated spectra were fitted assuming that the contributions arise from the first coordination shell of nearest neighbors surrounding the Cu impurity. For each structural model we calculated the theoretical EXAFS signals independently and fit the theory to the data. On the basis of the quality of the obtained fits and the physical meaning of the best-fit values of the adjustable parameters, we confirmed experimentally that the Cu is not a substitutional dopant, whereas the fits obtained based on the interstitial structural models yielded the best overall results. Concerning the two proposed interstitial sites (hexagonal and tetrahedral), the best fit was obtained for an interstitial hexagonal position. The best-fit results, presented in Figure 4, were obtained by simultaneously fitting the Cu K-edge k^3-weighed $\chi(k)$ data for the different doping levels of 200, 560, 800, and 1600 Cu impurities (Figure 4a–d, respectively) with the structural model of the Cu occupying an interstitial hexagonal site.

The Cu–As and Cu–In coordination numbers obtained by the fitting process, using the interstitial hexagonal model, confirm our prediction made based on visual examination of the XANES data. The best-fit values of the coordination numbers (Table 1) and the interatomic distances (~2.5 Å to either of the neighboring host atoms) are both consistent with this model (Figure 3e). The deviation of the coordination numbers, N, of Cu–In and Cu–As from the expected values of three may result from the assumptions of the model. (See the Supporting Information for more details.)

The feasibility of the suggested models for the Cu impurity configurations was further investigated using first-principle DFT calculations. First, to assess whether the Cu substitutes an In atom, we compared the energy difference of two configurations: A doped $In_{n-1}As_nCu$ lattice with a remote In atom and a neat In_nAs_n lattice with a remote Cu atom. From this, the energy required for a substitution of an In atom by a Cu impurity atom was found to be 0.39 eV, which suggests that the exchange of In with Cu is unlikely.

Next, we performed DFT calculations to examine several possible configurations for adding a Cu impurity into the InAs lattice. The energy required for a Cu to occupy a lattice site forcing the host In atom into an interstitial site (kick-out mechanism) was found to be 1.39 to 1.74 eV above the configuration in which the Cu occupies an interstitial site. The

dx.doi.org/10.1021/jp4032749 | J. Phys. Chem. C 2013, 117, 13688–13696

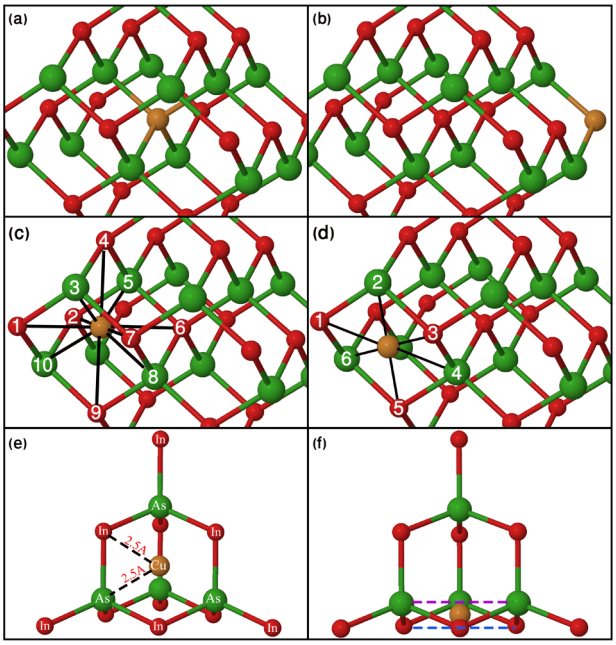

Figure 3. Illustrations of possible sites for a Cu (orange) impurity in an InAs (red, green respectively) NC. (a) Substitutional internal lattice site: $N_{(As)}$ = 4 and $r_{(Cu-As)}$ = 2.61 Å. (b) Substitutional surface site: $N_{(As)}$ = 3 and $r_{(Cu-As)}$ = 2.61 Å. (c) Interstitial tetrahedral site: The impurity is positioned at ([1/2, 1/2, 1/2]*a), where a = 6.04 Å for a zincblende structure. $N_{(As)}$ = 6, $N_{(In)}$ = 4, $r_{(Cu-In)}$ = 3.02 Å, and $r_{(Cu-As)}$ = 2.61 Å. (c) Interstitial hexagonal site: The impurity is positioned at ([3/8, 3/8, 5/8]*a). $N_{(As)}$ = $N_{(In)}$ = 3 and $r_{(Cu-In)}$ = $r_{(Cu-As)}$ = 2.5 Å. The front-view (e) and side-view (f) illustrations of the interstitial hexagonal site for a zincblende unit-cell.

range of energies depends on whether the interstitial site is of hexagonal or tetrahedral symmetry.

The DFT calculations showed that the energy of a Cu atom occupying the hexagonal site is lower by 62 meV with respect to a Cu occupying a tetrahedral site. Furthermore. for this configuration, that is, for the most stable doping scenario where the Cu impurity resides at a hexagonal interstitial site, we found that it is 2.86 eV lower compared with a remote Cu atom exterior to the InAs lattice. This indicates that the Cu impurity is strongly stabilized inside the NC; that is, the doping of the InAs NCs with Cu is expected to take place and self-purification[26] is unlikely.

The DFT calculations are in agreement with the experimental results in which Cu is an interstitial dopant occupying the hexagonal site. However, the energy difference between hexagonal and tetrahedral sites, as calculated from the DFT (62 meV), would suggest that at room temperature a few percent of the impurities may occupy tetrahedral sites.

The interstitial location of the Cu impurities is found to also gradually affect the nearest environment of the In and As atoms upon increasing dopant concentration. Remarkably, the XAFS data are consistent with a one-step transformation from pure to doped InAs NCs shown using an LCA. The LCA was performed independently for each edge (In and As) as well as for both XANES and EXAFS portions of the data. Figure 5a,c shows the two end states of the system represented by the pure InAs NC (solid lines) and the 2500 Cu doping level (dashed lines). The data corresponding to these end states were used to fit the experimental spectra of all intermediate doping concentrations. Representative fits for the doping level of 560 Cu atoms per NC in solution are shown in Figure 5b,d. (See Figures S2 and S3 of the Supporting Information for other fits.) Figure 5e shows quantitative results for both As and In (EXAFS and XANES) LCA fits. These results bestow a high confidence in the mixing fractions obtained by the LCA because the analyses done for both XANES and EXAFS data yielded similar results for each edge. Furthermore, these results demonstrate that a larger fraction of As atoms are perturbed by the presence of Cu, already at the lower Cu concentrations, compared with the In atoms.

Nearly Saturated Doping Concentration – the Onset of Cu–Cu Interactions. As mentioned in the previous sections, the visual examination of the raw data (Figure 2f) indicated a qualitative change in the local structure around the Cu occurring between the doping levels of 1600 and 2500. All collected data for doping levels up to and including the 1600 feature a single peak at roughly the same position and, as consequently confirmed by our analysis, resulted from the cocontribution of Cu–As and Cu–In pairs to the EXAFS signal. The peak observed for the 2500 Cu doping level is shifted to lower r values and broadened (Figure 2f). These variations point to either a change in the structure of the surrounding As, In shell or to the change in the composition of that shell. The former possibility was ruled out by the fitting analysis using just Cu–As and Cu–In bonds, which was successful in fitting all lower doping concentrations. To investigate the possibility of the latter case, we assumed that

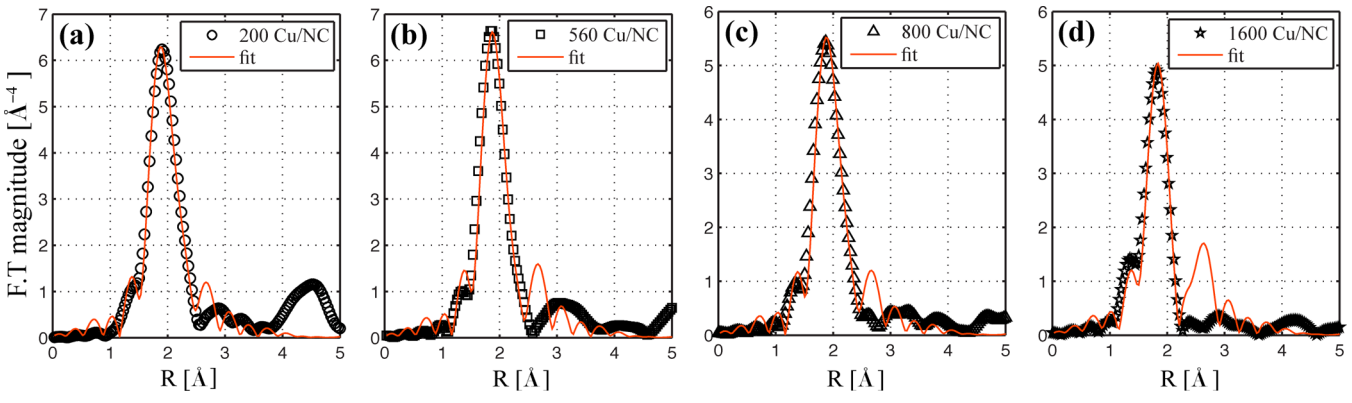

Figure 4. Fourier transform magnitudes of the Cu K-edge k^3-weighed EXAFS data (open symbols) of the 5 nm InAs NCs doped to the different levels (in solution). The solid lines represent the fits obtained using the structural model of a Cu impurity occupying only interstitial hexagonal sites.

dx.doi.org/10.1021/jp4032749 | J. Phys. Chem. C 2013, 117, 13688–13696

Table 1. Best-Fit Results for Structural Parameters of the Cu−As and Cu−In Nearest Neighbor Pairs Obtained by Cu K-Edge EXAFS Analysis for Various Cu Doping Levels (In Solution) of 5 nm InAs NCs

parameter	200 Cu/NC	560 Cu/NC	800 Cu/NC	1600 Cu/NC
N(Cu−As)	3.5 ± 0.3	4.2 ± 0.3	3.2 ± 0.3	3.9 ± 0.2
N(Cu−In)	1.7 ± 0.2	2.2 ± 0.2	1.5 ± 0.2	2.1 ± 0.1
r(Cu−As) [Å]	2.471 ± 0.005	2.493 ± 0.004	2.479 ± 0.006	2.502 ± 0.005
r(Cu−In) [Å]	2.451 ± 0.005	2.467 ± 0.004	2.457 ± 0.006	2.465 ± 0.005
σ^2(Cu−As) [Å^2]	0.007 ± 0.001	0.0074 ± 0.0007	0.0072 ± 0.0008	0.0083 ± 0.0008
σ^2(Cu−In) [Å^2]	0.0034 ± 0.0009	0.0038 ± 0.0006	0.0032 ± 0.0008	0.0047 ± 0.0007

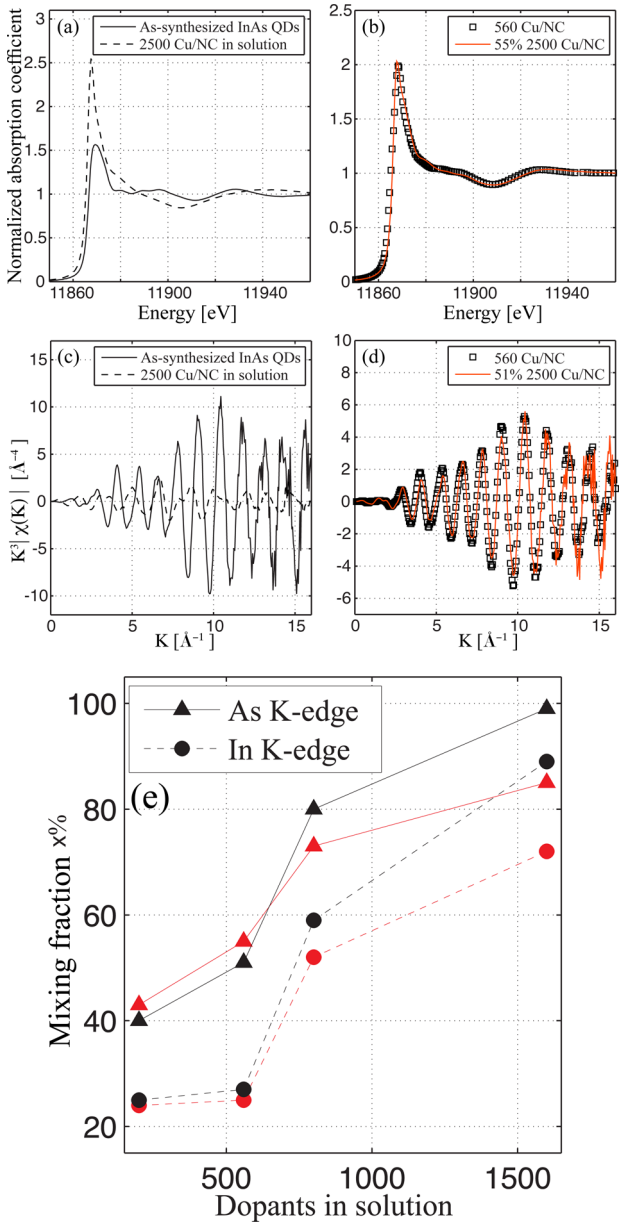

Figure 5. As K-edge XANES (a) and EXAFS (c) of the as-synthesized InAs NCs (solid line) and 2500 Cu/NC in solution (dashed line). Representative fits of XANES (b) and EXAFS (d) 560 Cu doping level data (□) via a linear combination analysis of the two end states. (e) Mixing fractions for the As K-edge XANES (red ▲), EXAFS (black ▲); and In K-edge XANES (red ●), EXAFS (black ●) as obtained for all intermediate doping levels.

the shift occurred due to the submixture of Cu−Cu pairs in the first coordination sphere. Theoretical EXAFS signals including Cu−In, Cu−As, and Cu−Cu contributions were reconstructed and fit to the experimental data.

Figure 6a,b, which, also shows the individual theoretical contributions of the different pairs, demonstrates the good fit in

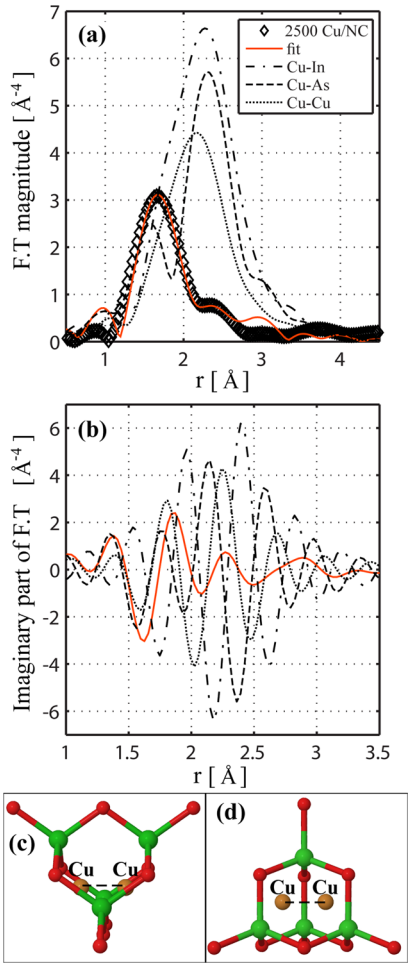

Figure 6. Fourier transform magnitudes of the k^3-weighed EXAFS data at the Cu K-edge (a) for the 2500 Cu atoms/NC sample (open symbols); the theoretical contributions of Cu−In (dotted-dashed), Cu−As (dashed), and Cu−Cu (dotted); and the resultant fit (red solid line). Imaginary part of the FT for the different contributing pairs and the resultant fit (b). Revised structural model for the nearly saturated level showing two Cu atoms occupying adjacent hexagonal sites in the same unit cell (c,d).

both magnitude and imaginary part of the FT, respectively. Table S3 in the Supporting Information contains the numerical results of the analysis. Indeed, as we suggested, Cu−Cu contribution was found to be significant. To check whether this contribution is a unique feature of this concentration only, we

dx.doi.org/10.1021/jp4032749 | J. Phys. Chem. C 2013, 117, 13688−13696

revisited the analysis of the lower Cu doping levels by adding Cu−Cu pairs to the fitted model. The best-fit results were obtained for negligible Cu−Cu contributions.

f

To explain the formation of the Cu−Cu pairs at the highest doping concentration, we consider the model depicted in Figure 6c,d. It is possible to fit up to four Cu atoms within hexagonal sites of the illustrated unit cell. The parameters obtained from the fit of the Cu−K edge EXAFS data to this model (Table S3 in the Supporting Information) show that each Cu atom is surrounded by ca. 2 other Cu atoms. The best-fit value for the Cu−Cu pair bond length of ∼2.45 Å is in agreement with previous EXAFS results showing a reduced metal−metal interatomic distance for small clusters with respect to their bulk counterparts.[54,55] This conclusion is further studied by powder XRD data (Figure 7), showing a

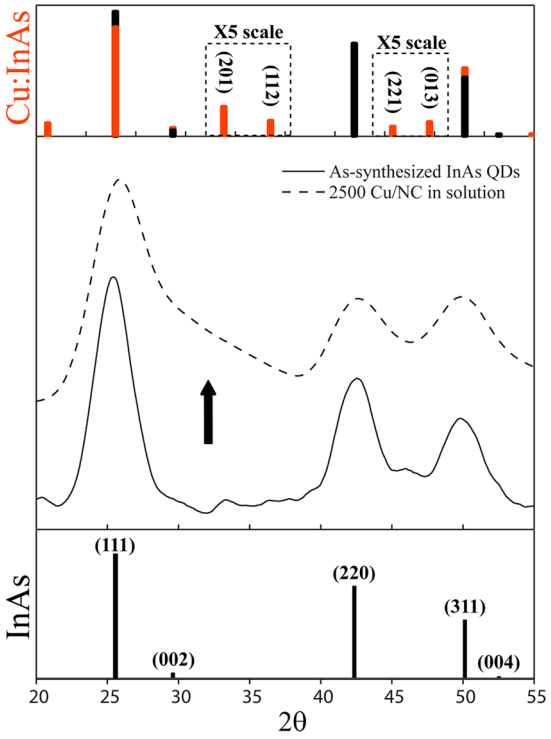

Figure 7. XRD diffractograms of as-synthesized 5 nm InAs NCs (solid line) and 2500 Cu atoms/NC doping (dashed line). The theoretical diffraction peaks simulated for a pure InAs zincblende lattice (black bars) overlaid with the theoretical diffraction peaks simulated for an InAs unit cell doped with two Cu impurities (top frame, red bars).

distinct feature near the (111) zincblende peak (designated by the arrow), which was observed only for the Cu 2500 doping level. The expected location of X-ray diffraction peaks for the Cu:InAs structure is shown in the top of the Figure and consistent with this feature. (See the Supporting Information for details of the calculation.)

To further understand the emergence of Cu pairing occurring only at extremely high Cu concentrations, we have preformed DFT calculations assuming two impurities occupying the same supercell. In these calculations, we considered two electronic spin configurations, with the singlet being the ground state (∼0.5 eV lower than the triplet). We find that the energy cost to bring the two impurities to adjacent hexagonal sites compared with the energy when the two impurities are separated by 10 Å along the [111] direction is 0.21 eV. Furthermore, we find that when the two impurities occupy adjacent hexagonal sites the energy is lower by 0.23 eV compared with the case in which one of the Cu impurities resides in an adjacent tetrahedral site. This suggests that only when the lattice is saturated and the Cu atoms are forced to be close to each other they will pair, which is in agreement with the experiments showing that at low Cu concentrations the probability of a single impurity atom per unit-cell increases.

CONCLUSIONS

The systematic study of diffusion-based Cu doping in presynthesized colloidal InAs NCs was carried out to determine the location of the impurity atoms within the NC lattice, the surrounding structure, and the concentration dependence. Advanced XAFS techniques yielded a structural model of Cu occupying an interstitial hexagonal impurity site inside the NC. This was reconfirmed using first-principle DFT calculations.

A gradual filling of the NC with Cu impurities takes place via a one-step transformation between the undoped and the nearly saturated NC. An interesting phenomenon is observed for the extremely high doping levels exhibiting interacting Cu−Cu impurities occupying adjacent interstitial lattice sites. The Cu pairing at high impurity concentration is also in good agreement with measured XRD and further justified by additional DFT calculations.

The results presented here provide conclusive evidence that Cu enters the InAs NC lattice and resides in a hexagonal interstitial site with good stability. This is consistent with our original findings that Cu leads to *n*-type doping of InAs NCs. The occupation of the interstitial site allows the Cu impurity to donate some of its charge to the NC, yielding the observed *n*-type character. Future directions will include a study for Ag dopants in InAs to provide a comprehensive structural analysis of this prototypical case of NC p-type doping.

ASSOCIATED CONTENT

Supporting Information

ICP-AES samples preparation and results of impurity concentration per NC, EXAFS fitting results for as-synthesized InAs NCs, further discussion on the EXAFS fitting of Cu-doped InAs NCs regarding the model assumption, and a detailed description of the XRD simulation process. This material is available free of charge via the Internet at http://pubs.acs.org.

AUTHOR INFORMATION

Corresponding Author

*E-mail: anatoly.frenkel@yu.edu; uri.banin@mail.huji.ac.il.

Notes

The authors declare no competing financial interest.

ACKNOWLEDGMENTS

We thank Reshef Tenne for connecting the team members together. The research leading to these results has received funding from the European Research Council under the European Union's Seventh Framework Programme (FP7/2007-2013)/ERC grant agreement no. 246841. A.I.F. and A.P. acknowledge the support of this work by the U.S. DOE Grant No. DE-FG02-03ER15476. X18B beamline is supported, in part, by Synchrotron Catalysis Consortium (U.S. DOE Grant No. DE-FG02-05ER15688). H.E. is grateful to The Center for Nanoscience and Nanotechnology at Tel Aviv University for a

postdoctoral fellowship. U.B. thanks the Alfred and Erica Larisch Memorial Chair.

REFERENCES

(1) Alivisatos, A. P. Perspectives on the Physical Chemistry of Semiconductor Nanocrystals. *J. Phys. Chem.* **1996**, *100*, 13226−13239.
(2) Brus, L. E. A Simple Model for the Ionization Potential, Electron Affinity, and Aqueous Redox Potentials of Small Semiconductor Crystallites. *J. Chem. Phys.* **1983**, *79*, 5566−5571.
(3) Murray, C. B.; Norris, D. J.; Bawendi, M. G. Synthesis and Characterization of Nearly Monodisperse CdE (E = Sulfur, Selenium, Tellurium) Semiconductor Nanocrystallites. *J. Am. Chem. Soc.* **1993**, *115*, 8706−8715.
(4) Guzelian, A. A.; Banin, U.; Kadavanich, A. V.; Peng, X.; Alivisatos, A. P. Colloidal Chemical Synthesis and Characterization of InAs Nanocrystal Quantum Dots. *Appl. Phys. Lett.* **1996**, *69*, 1432−1434.
(5) Murray, C. B.; Sun, S.; Gaschler, W.; Doyle, H.; Betley, T. A.; Kagan, C. R. Colloidal Synthesis of Nanocrystals and Nanocrystal Superlattices. IBM. *J. Res. Dev.* **2001**, *45*, 47−56.
(6) Coe, S.; Woo, W.-K.; Bawendi, M.; Bulovic, V. Electroluminescence from Single Monolayers of Nanocrystals in Molecular Organic Devices. *Nature* **2002**, *420*, 800−1−800−3.
(7) Gur, I.; Fromer, N. A.; Geier, M. L.; Alivisatos, A. P. Air-Stable All-Inorganic Nanocrystal Solar Cells Processed from Solution. *Science* **2005**, *310*, 462−465.
(8) Talapin, D. V.; Murray, C. B. PbSe Nanocrystal Solids for n- and p-Channel Thin Film Field-Effect Transistors. *Science* **2005**, *310*, 86−89.
(9) Lu, W.; Fang, J.; Ding, Y.; Wang, Z. L. Formation of PbSe Nanocrystals: A Growth Toward Nanocubes. *J. Phys. Chem. B* **2005**, *109*, 19219−19222.
(10) Jamie, H. W.; Huaqiang, C. Shape Control of PbS Nanocrystals Using Multiple Surfactants. *Nanotechnology* **2008**, *19*, 305605−1−305605−5.
(11) Rivest, J. B.; Swisher, S. L.; Fong, L.-K.; Zheng, H.; Alivisatos, A. P. Assembled Monolayer Nanorod Heterojunctions. *ACS Nano* **2011**, *5*, 3811−3816.
(12) Mocatta, D.; Cohen, G.; Schattner, J.; Millo, O.; Rabani, E.; Banin, U. Heavily Doped Semiconductor Nanocrystal Quantum Dots. *Science* **2011**, *332*, 77−81.
(13) Sze, S. M.; Ng, K. K. In *Physics of Semiconductor Devices*; Wiley: Hoboken, NJ, 2006.
(14) Willardson, R. K.; Beer, A. C. In *Physics of III-V Compounds*; Willardson, R. K., Beer, A. C., Eds.; Semiconductors and Semimetals *4*; Academic Press: New York, 1968.
(15) Dalven, R. A Review of the Semiconductor Properties of PbTe, PbSe, PbS and PbO. *Infrared Phys.* **1969**, *9*, 141−184.
(16) Erwin, S. C.; Zu, L.; Haftel, M. I.; Efros, A. L.; Kennedy, T. A.; Norris, D. J. Doping Semiconductor Nanocrystals. *Nature* **2005**, *436*, 91−94.
(17) Norris, D. J.; Efros, A. L.; Erwin, S. C. Doped Nanocrystals. *Science* **2008**, *319*, 1776−1779.
(18) Soo, Y. L.; Huang, S. W.; Ming, Z. H.; Kao, Y. H.; Munekata, H.; Chang, L. L. III-V Diluted Magnetic Semiconductor: Substitutional Doping of Mn in InAs. *Phys. Rev. B* **1996**, *53*, 4905−4909.
(19) Efros, A. L.; Rashba, E. I.; Rosen, M. Paramagnetic Ion-Doped Nanocrystal as a Voltage-Controlled Spin Filter. *Phys. Rev. Lett.* **2001**, *87*, 206601-1−206601-4.
(20) Somaskandan, K.; Tsoi, G. M.; Wenger, L. E.; Brock, S. L. Isovalent Doping Strategy for Manganese Introduction into III-V Diluted Magnetic Semiconductor Nanoparticles: InP:Mn. *Chem. Mater.* **2005**, *17*, 1190−1198.
(21) Yang, P.; Song, C.; Lü, M.; Zhou, G.; Yang, Z.; Xu, D.; Yuan, D. Photoluminescence of Cu^{+}-Doped and Cu^{2+}-Doped ZnS Nanocrystallites. *J. Phys. Chem. Solids* **2002**, *63*, 639−643.
(22) Srivastava, B. B.; Jana, S.; Pradhan, N. Doping Cu in Semiconductor Nanocrystals: Some Old and Some New Physical Insights. *J. Am. Chem. Soc.* **2010**, *133*, 1007−1015.
(23) Skolnick, M. S.; Dean, P. J.; Pitt, A. D.; Ch, U.; Krath, H.; Deveaud, B.; Foulkes, E. J. Optical Properties of Copper-Related Centres in InP. *J. Phys. C: Solid State* **1983**, *16*, 1967−1985.
(24) Xie, R.; Peng, X. Synthesis of Cu-Doped InP Nanocrystals (d-dots) with ZnSe Diffusion Barrier as Efficient and Color-Tunable NIR Emitters. *J. Am. Chem. Soc.* **2009**, *131*, 10645−10651.
(25) Geyer, S. M.; Allen, P. M.; Chang, L.-Y.; Wong, C. R.; Osedach, T. P.; Zhao, N.; Bulovic, V.; Bawendi, M. G. Control of the Carrier Type in InAs Nanocrystal Films by Predeposition Incorporation of Cd. *ACS Nano* **2010**, *4*, 7373−7378.
(26) Choi, J.-H.; Fafarman, A. T.; Oh, S. J.; Ko, D.-K.; Kim, D. K.; Diroll, B. T.; Muramoto, S.; Gillen, J. G.; Murray, C. B.; Kagan, C. R. Bandlike Transport in Strongly Coupled and Doped Quantum Dot Solids: A Route to High-Performance Thin-Film Electronics. *Nano Lett.* **2012**, *12*, 2631−2638.
(27) Tuinenga, C.; Jasinski, J.; Iwamoto, T.; Chikan, V. In Situ Observation of Heterogeneous Growth of CdSe Quantum Dots: Effect of Indium Doping on the Growth Kinetics. *ACS Nano* **2008**, *2*, 1411−1421.
(28) Roy, S.; Tuinenga, C.; Fungura, F.; Dagtepe, P.; Chikan, V.; Jasinski, J. Progress toward Producing n-Type CdSe Quantum Dots: Tin and Indium Doped CdSe Quantum Dots. *J. Phys. Chem. C* **2009**, *113*, 13008−13015.
(29) Gul, S.; Cooper, J. K.; Corrado, C.; Vollbrecht, B.; Bridges, F.; Guo, J.; Zhang, J. Z. Synthesis, Optical and Structural Properties, and Charge Carrier Dynamics of Cu-Doped ZnSe Nanocrystals. *J. Phys. Chem. C* **2011**, *115*, 20864−20875.
(30) Pi, X. Doping Silicon Nanocrystals with Boron and Phosphorus. *J. Nanomater.* **2012**, 912903-1−912903-9.
(31) Turnbull, D. Formation of Crystal Nuclei in Liquid Metals. *J. App. Phys.* **1950**, *21*, 1022−1028.
(32) Edmond, J. T.; Hilsum, C. Heat Treatment Effects in Indium Arsenide. *J. Appl. Phys.* **1960**, *31*, 1300−1301.
(33) Dalpian, G. M.; Chelikowsky, J. R. Self-Purification in Semiconductor Nanocrystals. *Phys. Rev. Lett.* **2006**, *96*, 226802-1−226802-4.
(34) Chan, T. L.; Tiago, M. L.; Kaxiras, E.; Chelikowsky, J. R. Size Limits on Doping Phosphorus into Silicon Nanocrystals. *Nano Lett.* **2007**, *8*, 596−600.
(35) Stern, E. A.; Heald, S. M. In *Handbook of Synchrotron Radiation*; Koch, E. E., Ed.; North-Holland: Amsterdam, 1983.
(36) Cao; Banin, U. Growth and Properties of Semiconductor Core/Shell Nanocrystals with InAs Cores. *J. Am. Chem. Soc.* **2000**, *122*, 9692−9702.
(37) Ravel, B.; Newville, M. ATHENA, ARTEMIS, HEPHAESTUS: Data Analysis for X-Ray Absorption Spectroscopy Using IFEFFIT. *J. Synchrotron Radiat.* **2005**, *12*, 537−541.
(38) Newville, M. IFEFFIT: Interactive XAFS Analysis and FEFF Fitting. *J. Synchrotron Radiat.* **2001**, *8*, 322−324.
(39) Zabinsky, S. I.; Rehr, J. J.; Ankudinov, A.; Albers, R. C.; Eller, M. J. Multiple-Scattering Calculations of X-Ray-Absorption Spectra. *Phys. Rev. B* **1995**, *52*, 2995−3009.
(40) Perdew, J. P.; Burke, K.; Ernzerhof, M. Generalized Gradient Approximation Made Simple. *Phys. Rev. Lett.* **1996**, *77*, 3865−3868.
(41) Paolo, G.; Stefano, B.; Nicola, B.; Matteo, C.; Roberto, C.; Carlo, C.; Davide, C.; Guido, L. C.; Matteo, C.; Ismaila, D.; et al. QUANTUM ESPRESSO: A Modular and Open-Source Software Project for Quantum Simulations of Materials. *J. Phys. Condens. Mater.* **2009**, *21*, 395502-1−395502-19.
(42) Tauc, J. In *Amorphous and Liquid Semiconductors*; Plenum: New York, 1974.
(43) Abram, R. A.; Rees, G. J.; Wilson, B. L. H. Heavily Doped Semiconductors and Devices. *Adv. Phys.* **1978**, *27*, 799−892.
(44) Bianconi, A. In *X-ray Absorption. Principles, Application, Techniques of EXAFS, SEXAFS and XANES*; Koningsberger, D. C., Prins, R., Eds.; Wiley: New York, 1988; pp 573−662.
(45) Frenkel, A. I.; Kleifeld, O.; Wasserman, S.; Sagi, I. Phase Speciation by Extended X-ray Absorption Fine-Structure Spectroscopy. *J. Chem. Phys.* **2002**, *116*, 9449−9456.

(46) Kim, J. Y.; Rodriguez, J. A.; Hanson, J. C.; Frenkel, A. I.; Lee, P. L. Reduction of CuO and Cu_2O with H_2: H Embedding and Kinetic Effects in the Formation of Suboxides. *J. Am. Chem. Soc.* **2003**, *125*, 10684−10692.
(47) Wang, X.; Hanson, J. C.; Frenkel, A. I.; Kim, J.-Y.; Rodriguez, J. A. Time-Resolved Studies for the Mechanism of Reduction of Copper Oxides with Carbon Monoxide: Complex Behavior of Lattice Oxygen and the Formation of Suboxides. *J. Phys. Chem. B* **2004**, *108*, 13667−13673.
(48) Wang, Q.; Hanson, J. C.; Frenkel, A. I. Solving the Structure of Reaction Intermediates by Time-Resolved Synchrotron X-Ray Absorption Spectroscopy. *J. Chem. Phys.* **2008**, *129*, 234502-1−234502-7.
(49) Piovano, A.; Agostini, G.; Frenkel, A. I.; Bertier, T.; Prestipino, C.; Ceretti, M.; Paulus, W.; Lamberti, C. Time Resolved in Situ XAFS Study of the Electrochemical Oxygen Intercalation in $SrFeO_{2.5}$ Brownmillerite Structure: Comparison with the Homologous $SrCoO_{2.5}$ System. *J. Phys. Chem. C* **2010**, *115*, 1311−1322.
(50) Frenkel, A. I.; Wang, Q.; Marinkovic, N.; Chen, J. G.; Barrio, L.; Si, R.; Cámara, A. L. P.; Estrella, A. M.; Rodriguez, J. A.; Hanson, J. C. Combining X-ray Absorption and X-ray Diffraction Techniques for in Situ Studies of Chemical Transformations in Heterogeneous Catalysis: Advantages and Limitations. *J. Phys. Chem. C* **2011**, *115*, 17884−17890.
(51) Solomon, E. I.; Randall, D. W.; Glaser, T. Electronic Structures of Active Sites in Electron Transfer Metalloproteins: Contributions to Reactivity. *Coord. Chem. Rev.* **2000**, *200*−*202*, 595−632.
(52) Soma, T.; Tahata, S.; Kagaya, H. M. Interstitial Atom in the Zincblende-Type Lattice. *Phys. Status Solidi B* **1990**, *157*, 509−518.
(53) Carlsson, A. E.; Zunger, A.; Wood, D. M. Electronic Structure of LiZnN: Interstitial Insertion Rule. *Phys. Rev. B* **1985**, *32*, 1386−1389.
(54) Frenkel, A. I.; Hills, C. W.; Nuzzo, R. G. A View from the Inside: Complexity in the Atomic Scale Ordering of Supported Metal Nanoparticles. *J. Phys. Chem. B* **2001**, *105*, 12689−12703.
(55) Frenkel, A. I.; Nemzer, S.; Pister, I.; Soussan, L.; Harris, T.; Sun, Y.; Rafailovich, M. H. Size-Controlled Synthesis and Characterization of Thiol-Stabilized Gold Nanoparticles. *J. Chem. Phys.* **2005**, *123*, 184701-1−184701-6.